

# Magnetic domain wall depinning assisted by spin wave bursts

Seonghoon Woo<sup>1,2</sup>, Tristan Delaney<sup>1</sup> and Geoffrey S. D. Beach<sup>1\*</sup>

**Spin waves (SWs) in magnetic structures could potentially be exploited for high-speed, low-power magnonic devices for signal transmission<sup>1–4</sup> and magnetic logic<sup>5–9</sup> applications. The short wavelengths and high frequencies of dipole-exchange-mode SWs in metallic ferromagnets make them particularly suitable for nanoscale devices<sup>10–14</sup>. However, these same characteristics make generation and detection challenging due to the length-scale mismatch of conventional SW interfaces such as microwave striplines. Here we show numerically and experimentally that colliding domain walls (DWs) release energetic spin wave bursts that can couple to and assist depinning of nearby DWs. Hence, DWs can be used as stationary reservoirs of exchange energy that can be efficiently generated, manipulated, and used to release SWs on demand, which can subsequently be detected again using DWs. This work highlights a route towards integrating DWs and SWs for enhanced functionality in spintronics applications.**

A significant challenge to realizing nanoscale magnonic devices is readily generating and detecting large-amplitude dipole-exchange-mode SWs (DESWs)<sup>11,14,15</sup>. Directly coupling to DESWs requires a means of excitation and detection with a characteristic length scale of the order of the exchange length<sup>13</sup>. Since the spin texture in magnetic DWs varies on precisely this length scale<sup>16</sup>, DWs and SWs can directly interact. Propagating SWs experience a phase shift following transmission through a DW<sup>10,17</sup>, which can be exploited to manipulate SWs for logic functionality in, for example, SW interferometers<sup>8,18,19</sup>. It has also been predicted that SWs should impart momentum to DWs<sup>20–29</sup>, leading to a magnonic spin-transfer torque that could drive DW dynamics much like conventional current-induced spin-transfer torque<sup>30</sup>. Micromagnetic simulations have indeed demonstrated that SWs can be used to pump and resonantly drive DWs in magnetic nanowires<sup>13,20–23,26–29</sup>. Moreover, with the emerging interest in Dzyaloshinskii–Moriya interactions, it has been predicted that Dzyaloshinskii–Moriya interactions can facilitate SW-driven DW motion<sup>31</sup>. However, no experiment has yet detected such behaviours, due in part to the challenge in generating DESWs with an amplitude sufficient to drive DW motion in the presence of disorder and pinning under realistic conditions.

Here we show that DW annihilation can be used to generate localized, energetic SW bursts, which can be subsequently probed using another DW. We characterize the propagating SWs generated during DW annihilation, and show that their amplitude is orders of magnitude greater than can be achieved through direct field excitation. We find that propagating SWs exert a force on a stationary DW that can aid in its depinning, equivalent to an effective field of order 10 Oe. Finally, we directly confirm SW emission from DW annihilation by time-resolved inverse spin-Hall effect measurements. These results provide the first experimental

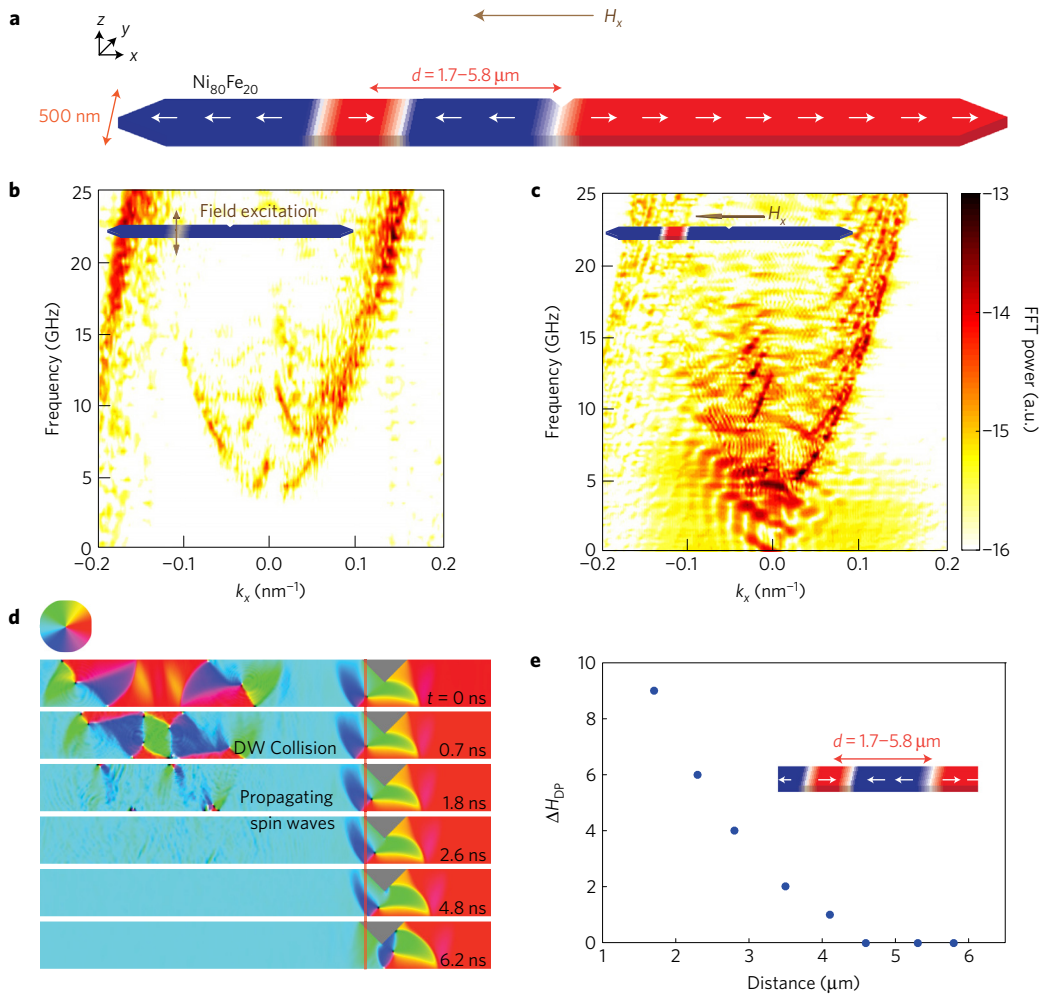
evidence that SWs can significantly affect DW dynamics and demonstrate that DWs can be used as both a source and detector of SWs in nanoscale magnetic devices.

Figure 1 summarizes micromagnetic simulations that motivate the experiments below. We examined SW bursts emitted during DW annihilation and their influence on a nearby stationary DW. The simulated geometry (Fig. 1a) consists of a Ni<sub>80</sub>Fe<sub>20</sub> nanowire with one DW pinned at a notch and a pair of DWs located a distance  $d$  away, which are driven by field to collide (see Methods). We first examined the propagating SW spectrum in the absence of DWs by applying a time-varying field  $H_y = H_0 \sin[2\pi\nu(t)]/[2\pi\nu(t)]$  to a region of cells centred 2.3  $\mu\text{m}$  to the left of the notch (see Methods). This serves to excite all SW modes up to a cutoff frequency  $\nu$  so as to reveal the accessible SW modes in the nanowire<sup>12</sup>. Figure 1b shows the excitation spectrum for  $\nu = 25$  GHz and  $H_0 = 10$  kOe obtained as the fast Fourier transform (FFT) of the time ( $t$ )-dependent  $z$ -component of magnetization  $m_z(t)$  along a 3- $\mu\text{m}$ -long region centred at the notch. The spectrum varies quadratically with wavevector  $k_x$  and exhibits a lower cutoff frequency related to the lowest transverse standing wave mode  $k_y$ , as expected for laterally constrained DESWs<sup>11</sup>.

Figure 1c shows the excitation spectrum in the same region of the nanowire after field-driven annihilation of a pair of vortex DWs at  $d = 2.3$   $\mu\text{m}$  with no DW present at the notch. During DW annihilation, large-amplitude standing-mode SWs are excited in the vicinity of the collision, and strong propagating SWs are emitted from this region as the local excitation damps out within a few nanoseconds. The SW emission is broadband and spectrally quite flat, and the radiated power (maximum FFT amplitude) is  $\sim 100$  times larger than produced by a 10 kOe local field excitation in Fig. 1b. The FFT power is independent of drive field amplitude, and hence the velocity of the colliding DWs, whereas it scales exponentially with  $H_0$  in the case of Oersted field excitation (see Supplementary Information 1 for details). Since DWs can be nucleated, propagated and annihilated with relatively low magnetic fields or spin-polarized currents, it is evidently far more efficient to create large-amplitude SWs by using DWs as local reservoirs of exchange energy, as opposed to directly exciting the SWs themselves.

The sequence of micromagnetic snapshots in Fig. 1d shows that the emitted SWs can impart momentum to a nearby DW and aid in its depinning. The threshold field required to depin the trapped DW in the absence of SW excitations was determined to be  $H_{\text{dp}}^* = 101$  Oe. In Fig. 1d, a field  $H_x = 95$  Oe was applied globally, after first initializing one vortex DW at the notch and a pair of vortex DWs centred  $d = 2.3$   $\mu\text{m}$  away from the notch. Since  $H_x < H_{\text{dp}}^*$ , the applied field alone is insufficient to depin the DW from the notch. However, following field application, the nearby DW pair collides and coalesces, emitting an intense SW

<sup>1</sup>Department of Materials Science and Engineering, Massachusetts Institute of Technology, Cambridge, Massachusetts 02139, USA. <sup>2</sup>Center for Spintronics, Korea Institute of Science and Technology, Seoul 02792, Republic of Korea. \*e-mail: [gbeach@mit.edu](mailto:gbeach@mit.edu)



**Figure 1 | Micromagnetic simulations of spin wave emission.** **a**, A schematic of the permalloy nanowire used for simulations, showing a domain wall pinned at a notch and a pair of domain walls to the left whose annihilation is driven by the applied field  $H_x$ . **b**, Fast Fourier transform (FFT) power spectrum of the z-component of the magnetization in a 3- $\mu\text{m}$ -wide region centred at the notch, for direct field excitation in the absence of domain walls, using a sine cardinal driving field waveform with amplitude  $H_0 = 10\ \text{kOe}$ . **c**, FFT power spectrum of the z-component of the local magnetization in the same region of the nanowire after field-driven annihilation of a pair of vortex DWs at  $d = 2.3\ \mu\text{m}$ . **d**, Sequence of micromagnetic snapshots showing collision and annihilation of a pair of vortex DWs, and the resulting propagating spin wave burst that assists the depinning of the domain wall at the notch, under a global driving field  $H_x = 95\ \text{Oe}$ . **e**, Reduction of the depinning field,  $\Delta H_{\text{DP}}$ , versus distance between the annihilation position and the notch.

burst. The DW-pair annihilation process occurs within  $\sim 1.8\ \text{ns}$ , during which time the pinned DW is minimally perturbed. This indicates that magnetostatic interactions between the pinned DW and the colliding DW pair have little influence on the depinning process. However, on arrival of large-amplitude SWs from the point of collision, the pinned DW is dragged and stretched along the SW propagation direction until a vortex core passes the notch at  $t \approx 5\ \text{ns}$  (Fig. 1d). After SW-assisted depinning, the DW then propagates rightward, driven by the applied magnetic field.

To quantify the influence of the SW burst on DW depinning, we determined the threshold field  $H_{\text{DP}}^{\text{SW}}$  required to depin the DW when a DW pair is annihilated nearby. Figure 1e plots the reduction of the depinning field,  $\Delta H_{\text{DP}} = H_{\text{DP}}^* - H_{\text{DP}}^{\text{SW}}$ , due to DW-pair annihilation as a function of  $d$ . It can be seen that SWs act as an effective field in depinning the DW, with a magnitude that is surprisingly large. At  $d = 1.7\ \mu\text{m}$ , the SW burst reduces the depinning threshold by  $\approx 9\ \text{Oe}$ , and although  $\Delta H_{\text{DP}}$  falls off rapidly with  $d$  due to the relatively short SW attenuation length, the influence on the depinning process remains significant at distances well beyond  $2\ \mu\text{m}$ .

We confirmed the predicted behaviour experimentally using the device configuration in Fig. 2. Experiments were performed on L-shaped  $\text{Ni}_{80}\text{Fe}_{20}$  nanowires with curved corners, where a notch

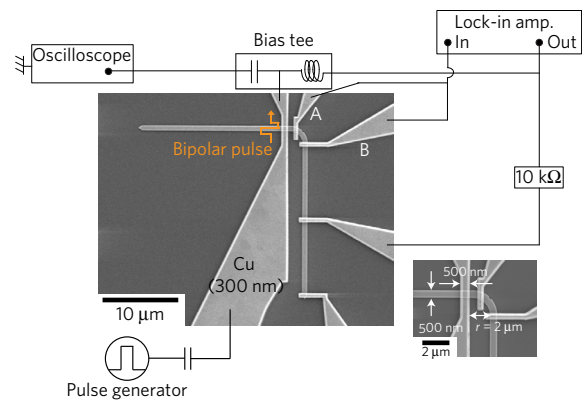


**Figure 2 | Device and experiment schematic.** A scanning electron micrograph of a nanowire device with electrical contacts and a domain wall nucleation/annihilation line, together with a schematic showing the instrument connections. The contacts labelled 'A' and 'B' are used for resistance measurement to detect the presence or absence of a DW at the corner. The panel in the bottom, right corner shows a magnified view of the corner, where the notch and dimensions are more clearly visible.

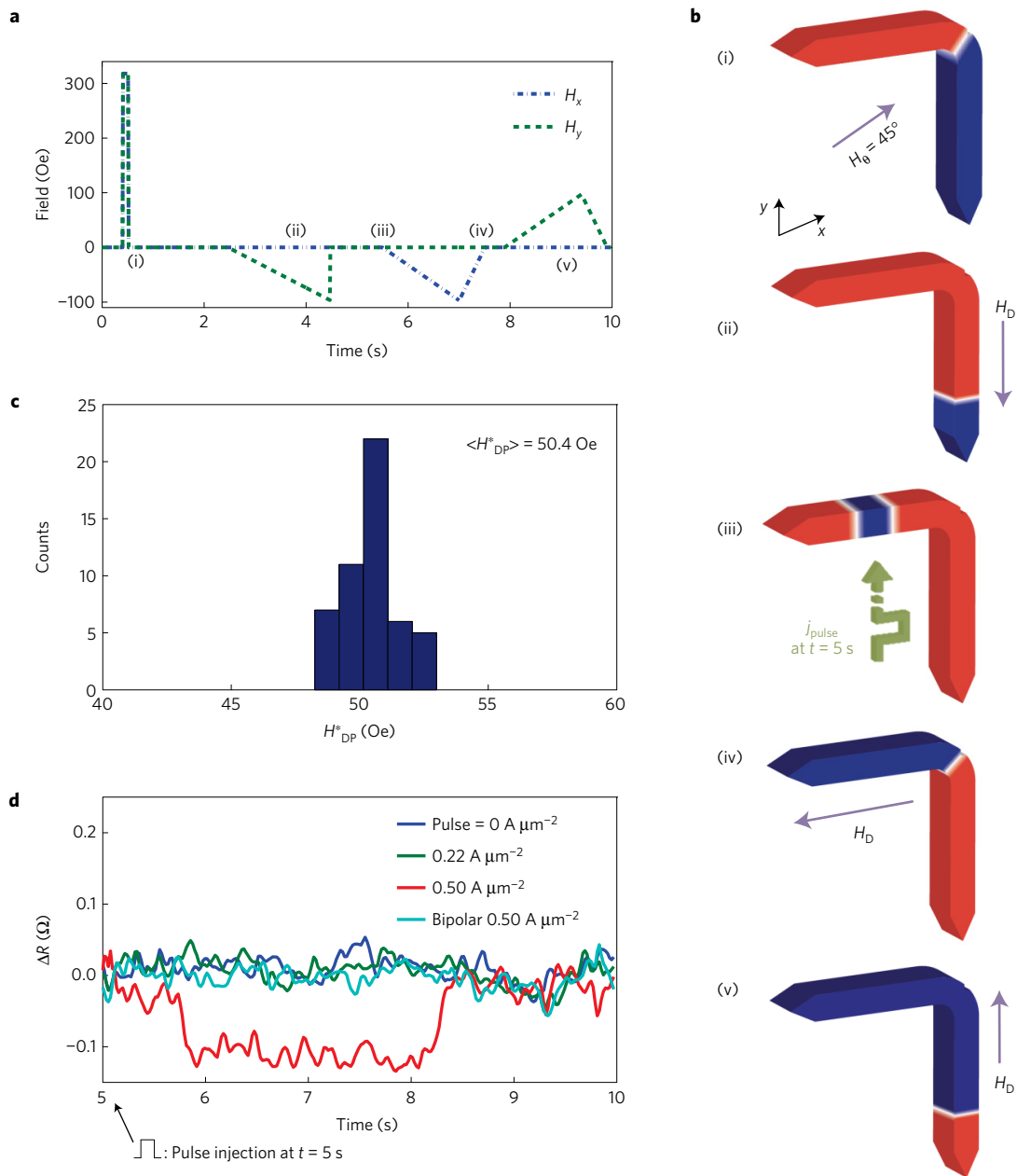


**Figure 3 | Characterizing domain wall depinning, nucleation and annihilation.** **a**, The magnetic field sequence used for determining the domain wall depinning and nucleation/annihilation thresholds. **b**, Schematics showing the field orientations at various points in the sequence, indicated in **a**. Schematic (iii) indicates injection of a single (uni- or bipolar) current pulse of density  $j_{\text{pulse}}$  through the nucleation/annihilation line. **c**, Histogram showing distribution of domain wall depinning field, measured using a swept field  $H_y$  along the  $y$  axis after first initializing a domain wall at the notch using a diagonally applied field. **d**, Variation in resistance at the nanowire corner with time during the portion of the field sequence indicated (iii)–(iv) in **b**. The different curves correspond to different amplitudes of the current pulse through the nucleation/annihilation line.

was patterned to serve as a pinning site. Current pulses were injected along a 500-nm-wide Cu stripline orthogonal to the NiFe nanowire, which generate a local in-plane Oersted field underneath the Cu stripe that was used to nucleate and annihilate DW pairs, a process studied in detail in ref. 32. DW depinning was detected electrically via the anisotropic magnetoresistance (AMR) measured across the notch<sup>33</sup>. The curved wire geometry allows a DW to be conveniently initialized at the notch using a diagonal applied field (Fig. 3a-(i)), and permits both DW depinning and nucleation/annihilation under the Cu stripe to be characterized independently using the field sequences described below. Our micromagnetic simulations (see Supplementary Information 3) confirm that the excitation spectrum and SW amplitudes generated by DW annihilation in a curved wire

are qualitatively similar to those in straight wires, consistent with ref. 19. Although the curved geometry can have some influence on the propagating SWs<sup>34–36</sup>, the simulations in straight nanowires in Fig. 1 should be reasonably predictive of the behaviour in the experimentally more convenient curved geometry.

We first separately characterized field-driven DW depinning from the notch, and local DW nucleation/annihilation underneath the Cu stripline. To determine the DW-depinning field  $H_{\text{DP}}^*$ , a DW was first initialized at the notch using a diagonal field of  $\approx 450$  Oe (Fig. 3a-(i)), and then displaced from the notch by a swept field  $H_y$  along the  $-\hat{y}$  axis (Fig. 3a-(ii)). The resistance across the notch dropped by  $\Delta R \sim 0.1 \Omega$  after applying the initialization field, consistent with the AMR from a nucleated DW. The resistance

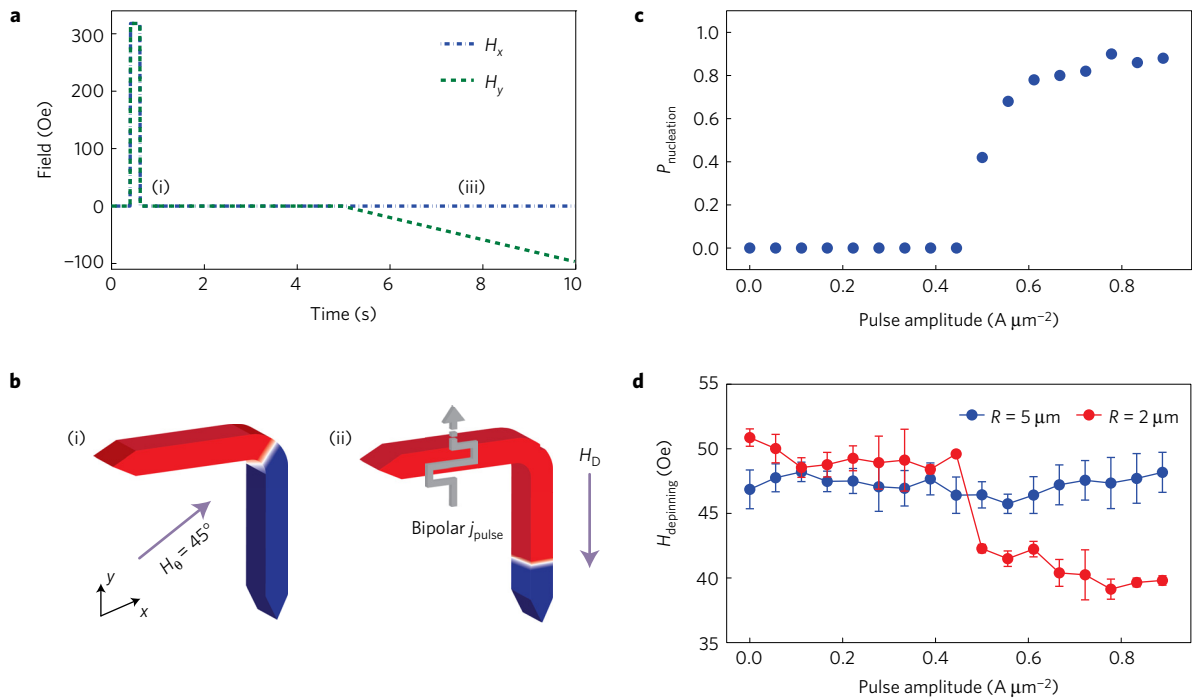


**Figure 4 | Experimental detection of domain wall depinning assisted by spin wave bursts.** **a**, The magnetic field sequence used to initialize a DW at the corner and then sweep the field along  $H_y$  to determine the depinning threshold. **b**, Schematics showing the steps in the field sequence. Beginning at  $t = 5$  s, bipolar current pulses are injected at a repetition rate of 10 kHz through the nucleation/annihilation line. **c**, Nucleation probability beneath the nucleation/annihilation line as a function of injected current density amplitude  $|j_{\text{pulse}}|$ , measured as described in the main text. **d**, Average depinning field versus  $|j_{\text{pulse}}|$  measured using the field sequence in **a**, while simultaneously injecting current pulses in the nucleation/annihilation line. Data are shown for nanowires with radius of curvature  $R = 2 \mu\text{m}$  and  $5 \mu\text{m}$ , corresponding to a distance from the notch to the centre of the nucleation/annihilation line of  $d = 2.3 \mu\text{m}$  and  $5.3 \mu\text{m}$ , respectively. The error bars in **d** represent calculated standard deviations from 50 measurements.

increased sharply back to its initial value as  $H_y$  was subsequently swept, corresponding to DW depinning and propagation away from the corner once  $H_y$  exceeds  $H_{\text{DP}}^*$ . Figure 3c shows a histogram of  $H_{\text{DP}}^*$  obtained from 50 depinning measurements, which exhibits a relatively narrow distribution around  $\langle H_{\text{DP}}^* \rangle \approx 50$  Oe. As expected, the experimental depinning field is much smaller than the zero-temperature simulation result,  $H_{\text{DP-Simul}} \approx 101$  Oe, due to thermally activated domain wall motion.

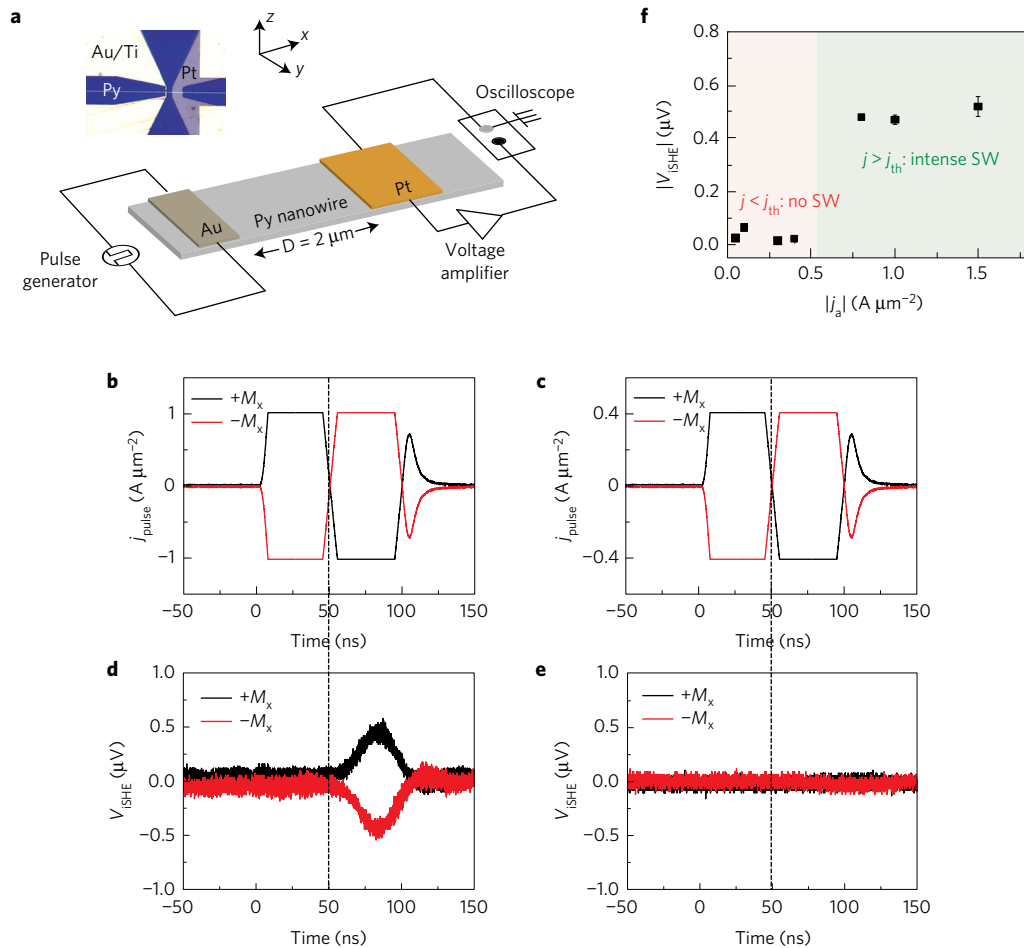
Figure 3d shows measurements used to characterize the current-pulse threshold in the Cu stripe necessary to nucleate and annihilate DW pairs. Here, the full field sequence shown in Fig. 3a,b was applied while monitoring the AMR signal (Fig. 3d). After first initializing the nanowire into a single-domain configuration (steps (i), (ii) in Fig. 3b), a 200-ns-wide current pulse was injected through the Cu stripline with a polarity such that the Oersted field opposes the magnetization direction directly beneath the stripe<sup>37,38</sup>. A field was then swept first along  $-\hat{x}$  and then along  $+\hat{y}$  corresponding to (iv) and (v), respectively, in Fig. 3b, so that if a reverse domain was nucleated by the pulse, a DW would be driven to the corner of the nanowire and then down the lower branch. The range over which  $H_x$  and  $H_y$  were swept was kept below the nucleation threshold of the nanowire, so that if the current pulse did not nucleate a reverse domain, the nanowire would remain in the single-domain state throughout the field cycle.

Figure 3d shows the AMR signal recorded during steps (iii)–(v) in the field sequence of Fig. 3a, for current pulses of several current densities. With no injected pulse, the AMR remains zero throughout the sequence, indicating the absence of a DW at the corner during the entire field cycle. Likewise, for a current density  $j_{\text{pulse}} = 0.22 \text{ A } \mu\text{m}^{-2}$  the AMR signal remains flat, indicating that the current-pulse amplitude remains below the local nucleation threshold. However, with  $j_{\text{pulse}} = 0.5 \text{ A } \mu\text{m}^{-2}$ , an AMR step is

observed at  $\approx 5.8$  s in Fig. 3d, corresponding to  $H_x = -20$  Oe as seen in the field waveform plotted in Fig. 3a. The steps in the AMR signal indicate that a reverse domain was nucleated under the Cu line and a DW was driven to the corner by  $H_x$  so that the resistance drops by  $\Delta R$ . The resistance then returns to its original value as the DW is swept downward by  $H_y$ , and away from the nanowire corner. When instead of a unipolar pulse, a bipolar current pulse with  $|j_{\text{pulse}}| = 0.5 \text{ A } \mu\text{m}^{-2}$  was injected, no AMR signal was detected during the swept field sequence (Fig. 3d), indicating that the DW pair generated by the positive-going pulse is subsequently annihilated by the negative-going pulse. The Cu stripline can hence be used to locally create and annihilate DW pairs using bipolar current pulses so long as  $|j_{\text{pulse}}|$  exceeds a threshold as determined below<sup>39</sup>.

Figure 4 summarizes experiments demonstrating that DW-pair annihilation underneath the Cu stripe assists DW depinning from the notch. Here, the field sequence shown in Fig. 4a,b was used to first initialize a DW at the notch and then measure the depinning field by sweeping  $H_y$  while monitoring the AMR. Prior to these measurements, the domain nucleation probability  $P_{\text{nuc}}$  underneath the Cu stripe was measured as a function of  $|j_{\text{pulse}}|$ , using unipolar pulses injected during measurements as described in Fig. 3d. The nucleation probability was determined from 50 consecutive measurements at each  $j_{\text{pulse}}$ , and is plotted in Fig. 4c. We observe a sharp nucleation threshold at  $|j_{\text{pulse}}| \approx 0.45 \text{ A } \mu\text{m}^{-2}$ , although  $P_{\text{nuc}}$  remains  $< 1$  up to the maximum pulse amplitude applied. We then repeated this experiment using bipolar pulses and found that DWs were never swept to the corner by  $H_x$  in step (iv) in Fig. 3b, indicating that the annihilation threshold is always less than the nucleation field. Hence, whenever a bipolar pulse generates a reversed domain, a DW annihilation event also occurs.

Figure 4d shows the depinning field  $H_{\text{DP}}$  from the notch, measured versus  $|j_{\text{pulse}}|$  for devices with two different radii of curvature



**Figure 5 | Direct electrical detection of spin waves via the inverse spin-Hall effect.** **a**, Schematic illustration of a permalloy nanowire with a Au domain wall nucleation stripe and a Pt inverse spin-Hall detector stripe. An actual device image taken by an optical microscope is shown in the inset. The Py and Au wires are 500 nm wide, and Pt is 5 μm wide. The distance between the Au and Pt edges is 2 μm. **b, c**, Bipolar pulse profiles with each pulse 50 ns long at  $|j_{\text{pulse}}| = 1.0 \text{ A } \mu\text{m}^{-2}$  (**b**) and  $|j_{\text{pulse}}| = 0.4 \text{ A } \mu\text{m}^{-2}$  (**c**). Small reflected pulses are observed after  $t = 100$  ns, due to the impedance mismatch. **d, e**, Time-resolved inverse spin-Hall effect voltage signals acquired with a time-resolved oscilloscope across the Pt stripe deposited on Py nanowires. For  $|j_{\text{pulse}}| > |j_{\text{th}}|$  (**d**), finite voltage is measured to be  $\approx 0.5 \mu\text{V}$  while no voltage signal is detected for  $|j_{\text{pulse}}| < |j_{\text{th}}|$  (**e**). The dashed lines indicate  $t = 50$  ns, where reversed magnetic field starts to drive and annihilate two domain walls for  $|j_{\text{pulse}}| > |j_{\text{th}}|$ . **f**, Ten-times averaged inverse iSHE voltage as a function of  $|j_{\text{pulse}}|$ , injected along the Au nucleation/annihilation line. The error bars in **f** represent calculated standard deviations from 10 measurements.

R. Here current pulses were injected at a repetition rate of 10 kHz, which is much faster than the field sweep rate during the depinning measurement. This high repetition rate ensures a high rate of DW nucleation/annihilation events whenever  $P_{\text{nuc}}$  becomes finite. For  $R = 2 \mu\text{m}$ , such that the distance  $d$  between the notch and the midpoint of the Cu stripe is  $d \approx 2.3 \mu\text{m}$ ,  $H_{\text{DP}}$  drops abruptly by  $\Delta H_{\text{DP}} \approx 9 \text{ Oe}$  above a threshold  $|j_{\text{pulse}}| \approx 0.45 \text{ A } \mu\text{m}^{-2}$  coinciding with the nucleation threshold beneath the Cu stripe. When  $d$  is increased to 5 μm (Fig. 4d), on the other hand, DW annihilation no longer measurably affects  $H_{\text{DP}}$ , as expected due to the short SW attenuation length of a few micrometres in permalloy<sup>15</sup>. These behaviours are qualitatively consistent with the influence of SW bursts on DW depinning predicted in the simulations in Fig. 1. The experimental value of  $\Delta H_{\text{DP}}$  is very close to the value  $\approx 6 \text{ Oe}$  predicted micromagnetically (Fig. 1e) for  $d \approx 2.3 \mu\text{m}$ ; quantitative differences may arise from the different material characteristics such as damping constant,  $\alpha$ , which significantly affects the SW attenuation, as well as finite temperature effects not included in the simulations.

Although the Oersted field generated by the Cu stripline could also influence  $H_{\text{DP}}$ , its contribution to  $\Delta H_{\text{DP}}$  should vary linearly with  $|j_{\text{pulse}}|$ . As seen in Fig. 4d,  $H_{\text{DP}}$  is independent of  $|j_{\text{pulse}}|$  below and above the nucleation/annihilation threshold, indicating

that the influence of the Oersted field on  $\Delta H_{\text{DP}}$  is far less than that of proximate DW-pair nucleation/annihilation. Moreover, considering the small current density  $\approx 6 \times 10^{-3} \text{ A } \mu\text{m}^{-2}$  flowing along a nanowire during the AMR measurement and the typical Joule heating-induced temperature rise,  $\Delta T = kJ^2$ , where  $k$  is approximately a few Kelvins per  $0.1 \text{ A } \mu\text{m}^{-2}$  for metals, Joule heating-induced thermal effects such as thermally driven DW motion<sup>40</sup> and thermal generation of SWs<sup>41</sup> can be neglected. We therefore conclude that SW generation by DW annihilation is dominantly responsible for the observed reduction in  $H_{\text{DP}}$ .

Finally, we directly detect the SWs bursts generated by DW annihilation utilizing the inverse spin-Hall effect (iSHE)<sup>42–44</sup>. We adopted a technique similar to that used recently to electrically detect travelling SWs in an yttrium iron garnet film<sup>43</sup>. In our experiments, shown schematically in Fig. 5a, a Pt stripe overlays a 500-nm-wide Py nanowire at a distance 2 μm away from a DW nucleation line. The Pt stripe serves as an iSHE detector (see Methods). We first measured the critical current density threshold,  $|j_{\text{th}}|$ , for DW nucleation via AMR measurements using the technique described in Fig. 3 (see Supplementary Information 5 for details). We found  $0.4 \text{ A } \mu\text{m}^{-2} < |j_{\text{th}}| < 0.8 \text{ A } \mu\text{m}^{-2}$  for this device, similar to the value of  $|j_{\text{th}}|$  measured for the DW-depinning devices described above.

The measurements then consisted of first saturating the nanowire magnetization along either  $+x$  or  $-x$ . Bipolar current pulses with profiles shown in Fig. 5b,c were then injected along the DW nucleation line with a polarity such that the first unipolar pulse generates an Oersted magnetic field oriented antiparallel to the Py magnetization. When  $|j_{\text{pulse}}| > |j_{\text{th}}|$  the bipolar pulse is therefore expected to nucleate and annihilate a pair of DWs. For  $|j_{\text{pulse}}| = 1.0 \text{ A } \mu\text{m}^{-2}$ , which exceeds  $|j_{\text{th}}|$  (Fig. 5b), a voltage pulse is detected at the Pt detector (Fig. 5d) with an amplitude  $\Delta V_{\text{ISHE}} \approx 0.5 \mu\text{V}$  after a delay of a few nanoseconds, which is consistent with the time required for the DWs to annihilate and the resulting SWs to reach the detector. When the Py layer is magnetized in the opposite direction, the sign of the detected voltage inverts as expected for the ISHE voltage<sup>42</sup>. When  $|j_{\text{pulse}}|$  is reduced below the DW nucleation threshold ( $0.4 \text{ A } \mu\text{m}^{-2}$  in Fig. 5c,e) no voltage signal is detected. As seen in Fig. 5f,  $|V_{\text{ISHE}}|$  abruptly vanishes below  $j_{\text{th}}$  and is constant for  $|j_{\text{pulse}}| > j_{\text{th}}$ . These observations, together with further systematic measurements described in Supplementary Information 6, establish the source of  $V_{\text{ISHE}}$  to be the SW burst generated through DW annihilation. This measurement constitutes the first direct observation of SWs generated by DW annihilation and supports our interpretation of the reduction in  $H_{\text{DP}}$  as being due to the influence of SWs on the depinning process.

We showed experimentally and computationally that SW bursts generated by DW collisions can couple to and drive a nearby DW, exerting a force comparable to an applied field of order 10 Oe. This sizable interaction shows that SWs can play an important role in DW dynamics and provides a new mechanism with which to manipulate DWs in nanoscale devices. DWs are well suited to non-volatile data storage<sup>33</sup>, but low propagation velocities can limit the signal transmission rate in DW logic circuits<sup>45</sup>. SWs by contrast offer high-speed, low-power signal transmission and logic operations<sup>5–7</sup>, but are difficult to generate and detect in nanoscale devices. By combining DWs and SWs in hybrid devices, non-volatility and integration with DW generation and readout mechanisms could be achieved while retaining high-speed operation and signal transmission in all-spin logic devices.

## Methods

Methods, including statements of data availability and any associated accession codes and references, are available in the [online version of this paper](#).

Received 11 February 2016; accepted 21 December 2016; published online 30 January 2017

## References

- Kajiwara, Y. *et al.* Transmission of electrical signals by spin-wave interconversion in a magnetic insulator. *Nature* **464**, 262–266 (2010).
- Gubbiotti, G. *et al.* Collective spin modes in monodimensional magnonic crystals consisting of dipolarly coupled nanowires. *Appl. Phys. Lett.* **90**, 092503 (2007).
- Chumak, A. V., Serga, A. A., Hillebrands, B. & Kostylev, M. P. Scattering of backward spin waves in a one-dimensional magnonic crystal. *Appl. Phys. Lett.* **93**, 022508 (2008).
- Kim, S.-K., Lee, K.-S. & Han, D.-S. A gigahertz-range spin-wave filter composed of width-modulated nanostrip magnonic-crystal waveguides. *Appl. Phys. Lett.* **95**, 082507 (2009).
- Kostylev, M. P., Serga, A. A., Schneider, T., Leven, B. & Hillebrands, B. Spin-wave logical gates. *Appl. Phys. Lett.* **87**, 153501 (2005).
- Khitun, A., Nikonov, D. E., Bao, M., Galatsis, K. & Wang, K. L. Feasibility study of logic circuits with a spin wave bus. *Nanotechnology* **18**, 465202 (2007).
- Schneider, T. *et al.* Realization of spin-wave logic gates. *Appl. Phys. Lett.* **92**, 022505 (2008).
- Lee, K.-S. & Kim, S.-K. Conceptual design of spin wave logic gates based on a Mach-Zehnder-type spin wave interferometer for universal logic functions. *J. Appl. Phys.* **104**, 053909 (2008).
- Jamali, M., Kwon, J. H., Seo, S.-M., Lee, K.-J. & Yang, H. Spin wave nonreciprocity for logic device applications. *Sci. Rep.* **3**, 3160 (2013).

- Hertel, R., Wulfhekel, W. & Kirschner, J. Domain-wall induced phase shifts in spin waves. *Phys. Rev. Lett.* **93**, 257202 (2004).
- Choi, S., Lee, K.-S., Guslienko, K. Y. & Kim, S.-K. Strong radiation of spin waves by core reversal of a magnetic vortex and their wave behaviors in magnetic nanowire waveguides. *Phys. Rev. Lett.* **98**, 087205 (2007).
- Lee, K.-S., Han, D.-S. & Kim, S.-K. Physical origin and generic control of magnonic band gaps of dipole-exchange spin waves in width-modulated nanostrip waveguides. *Phys. Rev. Lett.* **102**, 127202 (2009).
- Kim, S.-K. Micromagnetic computer simulations of spin waves in nanometre-scale patterned magnetic elements. *J. Phys. Appl. Phys.* **43**, 264004 (2010).
- Ulrichs, H., Demidov, V. E., Demokritov, S. O. & Urazhdin, S. Spin-torque nano-emitters for magnonic applications. *Appl. Phys. Lett.* **100**, 162406 (2012).
- Brächer, T. *et al.* Mode selective parametric excitation of spin waves in a  $\text{Ni}_{81}\text{Fe}_{19}$  microstripe. *Appl. Phys. Lett.* **99**, 162501 (2011).
- McMichael, R. D. & Donahue, M. J. Head to head domain wall structures in thin magnetic strips. *IEEE Trans. Magn.* **33**, 4167–4169 (1997).
- Bayer, C., Schultheiss, H., Hillebrands, B. & Stamps, R. L. Phase shift of spin waves traveling through a 180 deg; Bloch-domain wall. *IEEE Trans. Magn.* **41**, 3094–3096 (2005).
- Vasiliev, S. V., Kruglyak, V. V., Sokolovskii, M. L. & Kuchko, A. N. Spin wave interferometer employing a local nonuniformity of the effective magnetic field. *J. Appl. Phys.* **101**, 113919 (2007).
- Bance, S. *et al.* Micromagnetic calculation of spin wave propagation for magnetologic devices. *J. Appl. Phys.* **103**, 07E735 (2008).
- Han, D.-S. *et al.* Magnetic domain-wall motion by propagating spin waves. *Appl. Phys. Lett.* **94**, 112502 (2009).
- Jamali, M., Yang, H. & Lee, K.-J. Spin wave assisted current induced magnetic domain wall motion. *Appl. Phys. Lett.* **96**, 242501 (2010).
- Seo, S.-M., Lee, H.-W., Kohno, H. & Lee, K.-J. Magnetic vortex wall motion driven by spin waves. *Appl. Phys. Lett.* **98**, 012514 (2011).
- Wang, X., Guo, G., Nie, Y., Zhang, G. & Li, Z. Domain wall motion induced by the magnonic spin current. *Phys. Rev. B* **86**, 054445 (2012).
- Kim, J.-S. *et al.* Interaction between propagating spin waves and domain walls on a ferromagnetic nanowire. *Phys. Rev. B* **85**, 174428 (2012).
- Wang, X. S., Yan, P., Shen, Y. H., Bauer, G. E. W. & Wang, X. R. Domain wall propagation through spin wave emission. *Phys. Rev. Lett.* **109**, 167209 (2012).
- Wang, X., Guo, G., Zhang, G., Nie, Y. & Xia, Q. An analytical approach to the interaction of a propagating spin wave and a Bloch wall. *Appl. Phys. Lett.* **102**, 132401 (2013).
- Moon, K.-W., Chun, B. S., Kim, W. & Hwang, C. Control of domain wall motion by interference of spin wave. *J. Appl. Phys.* **114**, 123908 (2013).
- Tveten, E. G., Qaiumzadeh, A. & Brataas, A. Antiferromagnetic domain wall motion induced by spin waves. *Phys. Rev. Lett.* **112**, 147204 (2014).
- Hata, H., Taniguchi, T., Lee, H.-W., Moriyama, T. & Ono, T. Spin-wave-induced domain wall motion in perpendicularly magnetized system. *Appl. Phys. Express* **7**, 033001 (2014).
- Ralph, D. C. & Stiles, M. D. Spin transfer torques. *J. Magn. Magn. Mater.* **320**, 1190–1216 (2008).
- Wang, W. *et al.* Magnon-driven domain-wall motion with the Dzyaloshinskii-Moriya interaction. *Phys. Rev. Lett.* **114**, 087203 (2015).
- Stein, F.-U., Bocklage, L., Weigand, M. & Meier, G. Time-resolved imaging of nonlinear magnetic domain-wall dynamics in ferromagnetic nanowires. *Sci. Rep.* **3**, 1737 (2013).
- Parkin, S. S. P., Hayashi, M. & Thomas, L. Magnetic domain-wall racetrack memory. *Science* **320**, 190–194 (2008).
- Tkachenko, V. S., Kuchko, A. N., Dvornik, M. & Kruglyak, V. V. Propagation and scattering of spin waves in curved magnonic waveguides. *Appl. Phys. Lett.* **101**, 152402 (2012).
- Xing, X., Yu, Y., Li, S. & Huang, X. How do spin waves pass through a bend? *Sci. Rep.* **3**, 2958 (2013).
- Xing, X., Yin, W. & Wang, Z. Excitation of antisymmetric modes and modulated propagation of spin waves in bent magnonic waveguides. *J. Phys. Appl. Phys.* **48**, 215004–215010 (2015).
- Hayashi, M. *et al.* Dependence of current and field driven depinning of domain walls on their structure and chirality in permalloy nanowires. *Phys. Rev. Lett.* **97**, 207205 (2006).
- Prieto, J. L., Muñoz, M. & Martínez, E. Structural characterization of magnetic nanostrips by fast domain wall injection. *Phys. Rev. B* **83**, 104425 (2011).
- Stein, F.-U., Bocklage, L., Matsuyama, T. & Meier, G. Generation and annihilation of domain walls in nanowires by localized fields. *Appl. Phys. Lett.* **100**, 192403 (2012).
- Jiang, W. *et al.* Direct imaging of thermally driven domain wall motion in magnetic insulators. *Phys. Rev. Lett.* **110**, 177202 (2013).
- Uchida, K. *et al.* Observation of the spin Seebeck effect. *Nature* **455**, 778–781 (2008).

42. Saitoh, E., Ueda, M., Miyajima, H. & Tatara, G. Conversion of spin current into charge current at room temperature: inverse spin-Hall effect. *Appl. Phys. Lett.* **88**, 182509 (2006).
43. Chumak, A. V. *et al.* Direct detection of magnon spin transport by the inverse spin Hall effect. *Appl. Phys. Lett.* **100**, 082405 (2012).
44. Chumak, A. V., Vasyuchka, V. I., Serga, A. A. & Hillebrands, B. Magnon spintronics. *Nat. Phys.* **11**, 453–461 (2015).
45. Allwood, D. A. *et al.* Magnetic domain-wall logic. *Science* **309**, 1688–1692 (2005).

### Acknowledgements

This work was supported in part by C-SPIN, one of the six SRC STARnet Centers, sponsored by MARCO and DARPA. Technical support by D. Bono is gratefully acknowledged. Devices were fabricated using facilities in the MIT Nanostructures Laboratory, the Research Laboratory of Electronics and KIST Micro Fabrication Center. S.W. acknowledges support from the KIST institutional programme funded by Korea

Institute of Science and Technology. S.W. also acknowledges S. Emori for critical comments on the manuscript and financial support by the POSCO Science Fellowship of POSCO TJ Park Foundation and Kwanjeong Educational Foundation from South Korea.

### Author contributions

G.S.D.B. proposed and directed the study. S.W. and T.D. conducted micromagnetic simulations. S.W. and G.S.D.B. designed the experiments and S.W. carried out the experiments. S.W. and G.S.D.B. wrote the manuscript with input from T.D.

### Additional information

Supplementary information is available in the [online version of the paper](#). Reprints and permissions information is available online at [www.nature.com/reprints](http://www.nature.com/reprints). Correspondence and requests for materials should be addressed to G.S.D.B.

### Competing financial interests

The authors declare no competing financial interests.

## Methods

The micromagnetic simulations in the main text were carried out using the open-source MuMax3 developed by the group of B. Van Waeyenberge at Ghent University. The simulations in Supplementary Information 1 and 2 were carried out using the Object-Oriented MicroMagnetic Framework (OOMMF) developed by NIST. Material parameters were chosen appropriate for permalloy ( $\text{Ni}_{80}\text{Fe}_{20}$ ): Gilbert damping constant  $\alpha = 0.01$ , exchange constant  $A = 1.3 \times 10^{-11} \text{ J m}^{-1}$ , and saturation magnetization  $M_s = 8 \times 10^5 \text{ A m}^{-1}$ . The cell size was fixed at  $2.5 \times 2.5 \times 30 \text{ nm}^3$ . The nanowire geometry simulated in Fig. 1 is  $15 \mu\text{m}$  long,  $500 \text{ nm}$  wide, and  $30 \text{ nm}$  thick, with dimensions chosen to match the cross-sectional dimensions of the devices used in experiments. The nanowire includes tapered ends to prevent domain nucleation. The notch used to pin the domain wall is triangular with dimensions  $250 \text{ nm}$  deep and  $250 \text{ nm}$  long. The spin wave excitation spectrum in Fig. 1b was obtained by applying a time-varying field  $H_y = H_0 \sin[2\pi\nu t]/[2\pi\nu t]$  along the  $y$  axis to a region  $100 \times 500 \times 30 \text{ nm}^3$ , centred  $2.3 \mu\text{m}$  to the left of the notch. The excitation volume is chosen to be similar to the DW collision region that generates SWs in Fig. 1c. Each simulation in Fig. 1 was run for  $10 \text{ ns}$  and the data were recorded every  $\Delta t = 0.02 \text{ ns}$ .

Magnetic films used for DW-depinning experiments were prepared by d.c. magnetron sputtering at room temperature and  $2 \text{ mtorr}$  Ar pressure. The Permalloy nanowire consists of a Ta(2nm)/ $\text{Ni}_{80}\text{Fe}_{20}$ (30nm)/Ta(2nm) stack deposited on  $\text{SiO}_2$ (50nm)/Si substrate, patterned using electron beam lithography and ion milling with an Al hard mask, which was then removed by developer. Electrical

contacts and the domain wall nucleation line were then patterned from Ta(2nm)/Cu(300nm) films using a second layer of electron-beam lithography and lift-off. The notch used for DW depinning was  $\sim 100 \text{ nm}$  deep.

For the time-resolved measurement performed in Fig. 5, Permalloy nanowires were deposited on  $\text{SiO}_x$ (300nm)/Si substrates using d.c. magnetron sputtering at room temperature and then patterned into nanowires. Au and Pt stripes were deposited on top of Permalloy nanowires using an electron-beam lithography and lift-off. The Permalloy nanowire consists of Ta(2nm)/ $\text{Ni}_{80}\text{Fe}_{20}$ (30nm)/Ta(2nm), and the Au stripe Ti(5nm)/Au(100nm). To enhance the magnon-to-spin current conversion efficiency at the interface between Py and Pt, *in situ* Ar plasma cleaning at  $10 \text{ W}$  power was performed for 15 minutes under vacuum condition before depositing Pt. This interface improvement provides higher possibility to observe iSHE voltage by a factor of more than 150 as studied in ref. 46. For the low-noise time-resolved measurement, a voltage preamplifier and a low-pass filter were connected between the Pt stripe and oscilloscope.

**Data availability.** The data that support the plots within this paper and other findings of this study are available from the corresponding author on request.

## References

46. Jungfleisch, M. B., Lauer, V., Neb, R., Chumak, A. V. & Hillebrands, B. Improvement of the yttrium iron garnet/platinum interface for spin pumping-based applications. *Appl. Phys. Lett.* **103**, 022411 (2013).